

Full length article

Simulation and analysis of Au-MgF₂ structure in plasmonic sensor in near infrared spectral region

Anuj K. Sharma*

Department of Applied Sciences (Physics Division), National Institute of Technology Delhi, Narela, Delhi 110040, India

ARTICLE INFO

Article history:

Received 1 August 2017

Received in revised form 15 November 2017

Accepted 7 December 2017

Available online 18 December 2017

Keywords:

Plasmon

MgF₂

Sensor

Sensitivity

Infrared

ABSTRACT

Plasmonic sensor based on metal-dielectric combination of gold and MgF₂ layers is studied in near infrared (NIR) spectral region. An emphasis is given on the effect of variable thickness of MgF₂ layer in combination with operating wavelength and gold layer thickness on the sensor's performance in NIR. It is established that the variation in MgF₂ thickness in connection with plasmon penetration depth leads to significant variation in sensor's performance. The analysis leads to a conclusion that taking smaller values of MgF₂ layer thickness and operating at longer NIR wavelength leads to enhanced sensing performance. Also, fluoride glass can provide better sensing performance than chalcogenide glass and silicon substrate.

© 2017 Elsevier Ltd. All rights reserved.

1. Introduction

Plasmonics is one of the most widely applied areas of nanophotonics and possesses an exclusive setting for the manipulation of electromagnetic (EM) radiation *via* confinement of the corresponding EM field to the regions well below the diffraction limit. One particular domain where plasmonics has explored significant opportunities, and in which the sub-wavelength mode confines at nanoscale region, is the surface plasmon-based sensing technology. In simplest of the words, surface plasmons (SP) can be defined as quanta of coherent transverse magnetic (TM) oscillations of the surface charges at metal boundary [1]. SP-based optical sensors have been extensively used for highly sensitive and selective detection of various physical, chemical, and biological parameters [2–7].

The performance of any plasmonic sensor depends on the concerned metallic and dielectric media because they are the main drivers of how deep the SPs can be confined and how strongly they can interact with the incident EM field. In this view, there are ever-existing possibilities of improving performance of SPR-based sensors by, for example, introducing new materials, manipulating the light wavelength, and optimizing the thickness of media (primarily, metallic and dielectric) involved [8–10]. In this view, many two-dimensional (2D) dielectric materials with sub-atomic thickness and complex refractive index (*RI*) are being explored to

enhance the performance of photonic devices by manipulating the depth and interaction of SPs [11–13]. However, these 2D materials (e.g., graphene, MoS₂, MoSe₂) are still in the exploration stage and lot of information, such as dispersion relations in a large near infrared (NIR) spectral range (which is available in limited wavelength regions only [14,15]), is still to be produced for further implementation in SP-based devices and sensors, in particular.

In this context, other dielectric material layers such as SiO₂ [16] and MgF₂ [17] have been studied by exploring another similar phenomenon known as plasmon waveguide resonance (PWR) to enhance the sensitivity of plasmonic sensors. PWR is primarily defined as a method to enhance the evanescent field by increasing the thickness of dielectric layer (e.g., SiO₂, MgF₂ etc.) in order to couple the waveguide mode of dielectric layer with surface plasmon wave (SPW). The above study determined that MgF₂-based plasmonic sensor provided significantly superior performance than SiO₂-based sensor [17]. However, there are a few aspects that are yet to be explored. First, the above MgF₂-based plasmonic sensor was operated at single visible wavelength (633 nm) whereas MgF₂ is a dielectric medium showing encouraging optical properties in NIR also, therefore, the MgF₂-based SPR sensor should be explored in as large NIR spectral range as possible. This point is important in terms of the application of MgF₂-based sensor in determination of biosamples due to their much smaller photodamage in NIR range compared with visible wavelengths [19]. Therefore, an important objective should be to study the MgF₂-based plasmonic sensor in NIR leading to the development of sensor probe for important practical applications such as biosensing.

* Tel.: +91 11 33861252.

E-mail address: anujsharma@nitdelhi.ac.in

Apart from this, several key benefits can be achieved by moving into the IR regime like enhanced sensitivity, lower power requirements, and deeper penetration depth [20–22]. Second, because the penetration depth of SPW (which has a strong dependence on wavelength) is directly connected to the thicknesses of metallic and dielectric media involved, and strongly dictates the performance of plasmonic devices [23], the variation in thickness of dielectric MgF_2 layer should be explored in conjunction with metal layer thickness and operating wavelength in context of plasmonic sensor's performance. Furthermore, the role of different substrate materials active in NIR spectral region should also be investigated.

In this work, an Au- MgF_2 'metal-dielectric' configuration has been considered to analyze a plasmonic sensor in NIR spectral region. The sensed samples are taken as normal water (H_2O) and heavy water (D_2O) at room temperature. In order to optimize the sensor's performance, the analysis is carried out for a wide spectral range in NIR. As a very important performance tuning parameter, the effect of MgF_2 thickness is evaluated in combination with different thicknesses of Au layer. Further, the MgF_2 -based sensor's performance is analyzed and compared for important glass materials (chalcogenide, fluoride, and silicon) possessing favorable optical properties in NIR.

2. Theory and background

Proposed plasmonic sensor is based on Kretschmann configuration [24] and comprises of four layers (shown in Fig. 1): (i) light coupling substrate, (ii) metal layer, (iii) MgF_2 layer, and (iv) analyte.

Following equation represents the plasmon resonance condition:

$$\frac{2\pi}{\lambda} n_p \sin \theta_{\text{SPR}} = \text{real} \left(\frac{2\pi}{\lambda} \sqrt{\frac{\epsilon_m \epsilon_s}{\epsilon_m + \epsilon_s}} \right) \quad (1)$$

The left hand and right hand sides of Eq. (1) represent the wave vectors (along the interface) of incident TM light (monochromatic) and SPW, respectively. In above equation, ϵ_m and ϵ_s are, respectively, the dielectric constants of metallic and dielectric (analyte) media; n_p is RI of the light coupling substrate material; θ_{SPR} is the resonance angle of incidence; and λ is the wavelength of incident

light. On coupling of SPs with incident light, a narrow dip in resonance curve is obtained at the output having minimum (near zero) reflectance (R_{min}) at resonance angle (θ_{SPR}) as shown in Fig. 1. In the following sub-sections, different components of the sensor along with their properties and selection criteria are discussed:

2.1. Layer 1: Light coupling substrate

SPR-based structures in IR region have substantially different excitation parameters and support advantages for sensing applications in terms of high probe depth [20] and more precise determination of SPR dip [25]. For that matter, chalcogenide glasses based on the Group VI chalcogen elements (sulfur, selenium, and tellurium) have generated significant interest due to their transparent behavior in the IR region [26]. Substrates based on chalcogenide glass have advantage over silica glass owing to its higher thermal and chemical stability [26]. For the present study, $\text{As}_{40}\text{Se}_{60}$ chalcogenide glass has been considered as light coupling substrate. The wavelength-dependent RI of $\text{As}_{40}\text{Se}_{60}$ is taken into account [27].

2.2. Layer 2: Thin metal layer

Gold and silver encompass extraordinary optical properties supporting plasmonic devices due to strong free electron behavior [28]. Au is chosen as SPR active metal in the present study due to its high stability against oxidation, more efficient bonding with biochemical layers (e.g., thiol etc.) in comparison to silver [29], and the largest $\delta\theta_{\text{SPR}}$ among the other SPR active metals, e.g., Ag, Al and Cu [30,31]. Also, Au is preferred because highly polarized SPW is generated with enhanced evanescent wave [32]. For the present study, 40–65 nm thickness of Au layer is considered. The wavelength dependent dielectric constant of gold in NIR is considered for sensor simulations [33].

2.3. Layer 3: MgF_2 layer

An MgF_2 layer is considered to be sandwiched between Au layer and analyte sample. The previous studies show that MgF_2 is almost entirely immune to radiation damage in NIR [34]. This feature can

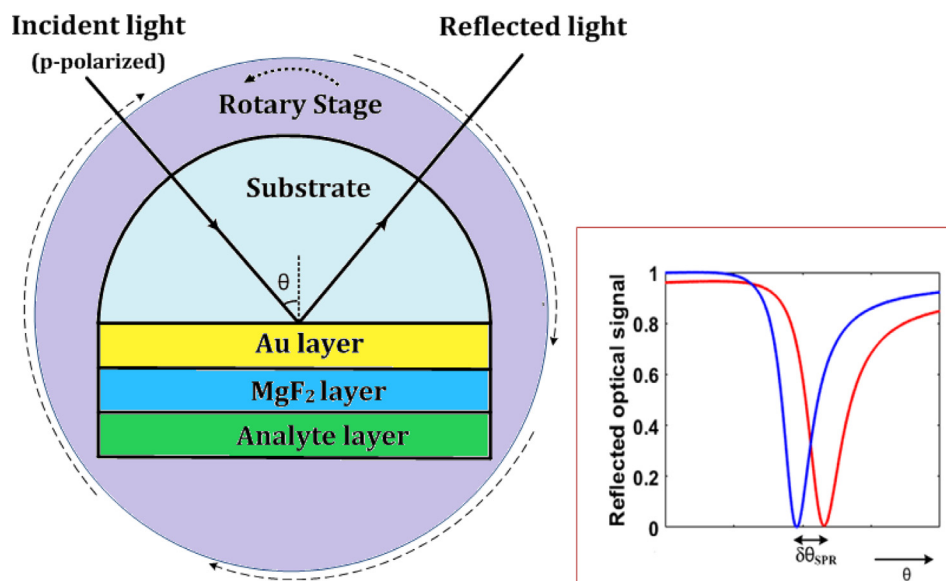


Fig. 1. Schematic of 4-layer Kretschmann configuration as an Au- MgF_2 'metal-dielectric' configuration based plasmonic sensor. The sensor structure is usually fixed on a rotary stage in order to carry out the sensing procedure under angular interrogation method. On the right hand, the corresponding resonance curve is depicted in which the reflected optical signal encounters a sharp dip at the resonance angle (θ_{SPR}), which shifts to some other angle value upon change in analyte. The angular shift in resonance curve is represented as $\delta\theta_{\text{SPR}}$.

be particularly useful in plasmonic biosensor operating at NIR wavelengths. MgF₂ also shows extremely small thermo-optic coefficient ($\sim 10^{-7}$ RIU/K) [35], which is useful in achieving stable sensor performance against temperature fluctuations. The corresponding wavelength dependences of RI of MgF₂ has been considered [18].

2.4. Layer 4: Analyte sample

In many of SPR sensor studies, the refractive index variation is taken as constant for multiple wavelengths, which may lead to non-precise results and conclusions. Therefore, for the present work, the analyte layer is considered as H₂O and D₂O samples being measured at room temperature. Their concerned dispersions, i.e. the variation of refractive index (real part ‘n_s’) and extinction coefficient (imaginary part ‘κ_s’) with wavelength, are taken into account [36]. The wavelength-dependent absorption of light by H₂O and D₂O samples is taken into account by carefully considering their corresponding extinction coefficients.

2.5. Transfer matrix method

The value of reflected output signal (R) should be calculated with high precision to avoid any errors in recording θ_{SPR} . Since the present structure is a multilayer one (i.e., substrate-Au layer-MgF₂ layer-analyte), so the transfer matrix method for N-layer structure is used in order to obtain ‘R’ for p-polarized incident beam. The matrix method is very accurate as it contains no approximations and has the ability, in generic form, to also include incoherent (thick layers) and partially coherent (rough surface or interfaces) reflection and transmission [37]. The matrix method facilitates highly precise calculations for various multilayer structures including buried insulating and conducting layers, and multilayers with a thick incoherent layer in any arbitrary position [37].

A basic N-layer optical system is shown in Fig. 2. The layers are stacked along the z-axis. The arbitrary medium layer is defined by thickness d_k , dielectric constant ϵ_k , permeability μ_k , and refractive index n_k .

The tangential fields at the first boundary $z = z_1 = 0$ are related to those at the final boundary $z = z_{N-1}$ by:

$$\begin{bmatrix} U_1 \\ V_1 \end{bmatrix} = M \begin{bmatrix} U_{N-1} \\ V_{N-1} \end{bmatrix} \tag{2}$$

where U_1 and V_1 , respectively, are the tangential components of electric and magnetic fields at the boundary of first layer. U_{N-1} and V_{N-1} are the corresponding fields at the boundary of N_{th} layer. M is known as characteristic transfer matrix of the combined structure given by:

$$M = \prod_{k=2}^{N-1} M_k \tag{3}$$

$$M_k = \begin{bmatrix} \cos \beta_k & (-i \sin \beta_k) / q_k \\ -i q_k \sin \beta_k & \cos \beta_k \end{bmatrix} \tag{4}$$

$$q_k = \left(\frac{\mu_k}{\epsilon_k} \right)^{1/2} \cos \theta_k = \frac{(\epsilon_k - n_1^2 \sin^2 \theta)^{1/2}}{\epsilon_k} \tag{5}$$

$$\beta_k = \frac{2\pi}{\lambda} n_k \cos \theta_k (z_k - z_{k-1}) = \frac{2\pi d_k}{\lambda} (\epsilon_k - n_1^2 \sin^2 \theta)^{1/2} \tag{6}$$

The amplitude reflection coefficient (r) for p-polarized light is given by

$$r = \frac{(M_{11} + M_{12}q_N)q_1 - (M_{21} + M_{22}q_N)}{(M_{11} + M_{12}q_N)q_1 + (M_{21} + M_{22}q_N)} \tag{7}$$

Finally, reflected optical signal (R) is calculated as:

$$R = |r|^2 \tag{8}$$

2.6. Performance evaluation parameter

As far as the performance of SPR sensor is concerned, it is required that FWHM (resonance curve width) should be as small and sensitivity ($\delta\theta_{SPR}/\delta n_s$) should be as large as possible for reliable SPR-based sensing [7]. For the present study, a single performance parameter, known as combined sensitivity factor (CSF), is employed [17,38].

$$CSF = \frac{\delta\theta_{SPR}}{\delta n_s} \times \frac{(R_{max} - R_{min})}{FWHM} \tag{9}$$

In above expression, δn_s is the difference between RI of normal and heavy water samples and $\delta\theta_{SPR}$ is the corresponding angular shift in resonance curve. Further, R_{max} and R_{min} are the normalized reflectance values representing, respectively, the highest and lowest points of the corresponding resonance curve. From above expression, the unit of CSF is RIU⁻¹.

2.7. Outline for simulation of sensor model

The study is based on angular interrogation method in which there is variation in resonance curve obtained with respect to incident angle (θ) at selected operating wavelength (λ). The model for proposed plasmonic sensor consists of:

- (i) A monochromatic light source (e.g., a laser beam source) with polarizer,
- (ii) Multilayered structure (i.e., Au and MgF₂ layers) deposited on glass substrate, which is fixed on a rotary stage (for angular interrogation), and
- (iii) Photodetector sensitive to the concerned wavelength range. In angular interrogation method, position sensitive detector (PSD) is used for the measurement of the angular shift in light beam [39].



Fig. 2. Schematic for N-layer transfer matrix method to calculate the reflected light intensity (R).

When a p-polarized (*i.e.*, TM) light beam of wavelength λ is considered to be incident through the light coupling substrate on the substrate-metal interface at an angle θ equal to or greater than the angle (θ_{ATR}) required for attenuated total reflection (ATR), the evanescent wave is generated at the substrate-metal interface. This evanescent wave acts as a medium to couple the incident light with SPW and leads to resonant excitation of SPs. If ' R ', which is the output signal under angular interrogation, is measured as a function of incident angle θ , then a sharp dip is observed at resonance angle θ_{SPR} (as shown in Fig. 1).

For calculating the SP penetration depth, the simulations were carried out using COMSOL Multiphysics software tool, which provides a one-dimensional (1D) as well as 2D distributions of the field in all the layers involved by considering their thicknesses, RI , and operating wavelength. For simulating resonance curve (with transfer matrix method) leading to CSF values under different design considerations (*e.g.*, for different thicknesses of Au and MgF₂ layers, and wavelengths), the Matlab® software is utilized.

3. Results and discussion

In this section, a sequenced discussion of the steps will be carried out leading to a sensor design with modalities for best possible performance.

3.1. Au thickness optimization vis-à-vis MgF₂ thickness and incident wavelength

For a large number of samples, the performance of a plasmonic sensor depends heavily on the depth of SPs into the adjacent media because larger the penetration depth, stronger the interaction of the field with analyte medium. Nevertheless, it is important to mention here that a more confined penetration depth corresponding to a similar field enhancement may be preferred in the monitoring of molecular interactions (in order to exclude the effect of bulk RI). Also, the thicknesses of the media forming the plasmonic junction (Au and MgF₂ in this case) and wavelength of incident light have very close connection in terms of radiation damping, which is broadly a term related to amount of light energy radiated back into the metal layer. Therefore, it is important to investigate what thickness combination of Au-MgF₂ junction and operating wavelength may lead to the best sensing performance. In this context, Fig. 3 depicts the optimization of Au thickness for different NIR wavelengths.

The above plots in Fig. 3 correspond to MgF₂ layer thickness of 200 nm. Two points stand out from the above diagram. First, the variation of CSF with Au thickness follows a certain trend, *i.e.*, CSF attains a maximum (peak) value at a particular Au thickness corresponding to each wavelength. With an increase in NIR wavelength, the optimized Au thickness (*i.e.*, corresponding to peak CSF) shifts to a smaller value. Numerically, the optimized Au thickness is 63 nm at $\lambda = 900$ nm, 56.4 nm at $\lambda = 1100$ nm, 51.7 nm at $\lambda = 1300$ nm, and 50.1 nm at $\lambda = 1500$ nm. Second, the sensor's overall performance, determined in terms of CSF, improves with an increase in NIR wavelength. It is clear from the figure that for any thickness of Au layer, the value of CSF is significantly higher for 1500 nm wavelength compared with other three NIR wavelengths. For instance, at 40 nm thickness of Au film, the CSF at $\lambda = 1500$ nm is about 10 times, 2.4 times, and 1.5 times higher than CSF values, respectively, at 900 nm, 1100 nm, and 1300 nm wavelength. This observation clearly indicates that it is appropriate to operate at longer NIR wavelengths to achieve enhanced performance from the plasmonic sensor. The enhanced plasmonic sensing performance at longer NIR wavelength has been reported previously also [20]. In that sense, the above outcome corroborates the results of

above-mentioned work [20] related to plasmonic sensor performance in NIR.

However, the above plots correspond to only a single value (200 nm) of MgF₂ layer thickness and it is also necessary to appreciate how the optimized Au thickness varies for different MgF₂ layer thickness. Following the aforementioned result regarding preferring longer NIR wavelength, the inset of Fig. 3 demonstrates the variations of (i) optimized Au thickness, and (ii) corresponding peak CSF with MgF₂ layer thickness at $\lambda = 1500$ nm. It is visible from the inset that for a fixed wavelength (*i.e.*, 1500 nm), the value of optimized Au thickness is different for each thickness of MgF₂ layer. The optimized Au thickness varies non-linearly from nearly 49 nm (for 50 nm thick MgF₂ layer) to 56 nm (for 600 nm thick MgF₂ layer). The right hand vertical axis represents the variation of peak CSF corresponding to each MgF₂ layer thickness. It is important to note that peak CSF decreases with an increase in MgF₂ layer thickness showing a non-linear fall from 133.75 RIU⁻¹ (for 50 nm thick MgF₂ layer) to 124.50 RIU⁻¹ (for 600 nm thick MgF₂ layer). It indicates that in order to achieve the best sensing performance, one has to carefully and simultaneously select the light wavelength, MgF₂ thickness, and Au thickness. From the discussion so far, it can be established that longer NIR wavelength, smaller MgF₂ thickness, and the corresponding optimized Au thickness may lead to significantly high sensing performance.

In order to meticulously establish the above optimization of the sensor's performance, the peak CSF is plotted at $\lambda = 1500$ nm for the considered full range of Au thickness (40–65 nm) and MgF₂ thickness (50–650 nm) as shown in Fig. 4.

While taking into account that longer NIR wavelength should be preferred (as discussed above and supported by the previous results [20]), the above structural variation of peak CSF confirms that smaller MgF₂ thickness and the corresponding optimized thickness of Au layer (*i.e.*, nearly 50 nm at $\lambda = 1500$ nm) leads to the maximum possible CSF value (133.75 RIU⁻¹). Nevertheless, the effect of MgF₂ thickness on other aspects of the plasmonic sensor based measurement must be analyzed in more detail in order to comprehensively evaluate the sensor's performance.

3.2. Analysis of resonance curves in view of MgF₂ layer thickness

Following the above discussion, Fig. 5 depicts the resonance curves at $\lambda = 1500$ nm for five different values (50 nm, 200 nm, 500 nm, and 650 nm) of MgF₂ layer thickness. It is visible from Fig. 5 that a variation in MgF₂ thickness significantly affects the parameters of resonance curve corresponding to same analyte: D₂O, same Au thickness (optimized): 50 nm, and at same wavelength: 1500 nm.

These parameters should be investigated in more elaboration to comprehensively analyze the overall effect of MgF₂ thickness on sensor's performance.

3.2.1. Sensitivity and detection limit

Sensitivity ($\delta\theta_{SPR}/\delta n_s$) of a plasmonic sensor should be as large as possible. The overall performance parameter (CSF) also takes this into account and is directly proportional to the sensitivity as per Eq. (9). For the present analysis, the shift in resonance curve for D₂O ($RI = 1.3174$ at $\lambda = 1500$ nm [25]) sample is measured with reference to H₂O sample ($RI = 1.3164$ at $\lambda = 1500$ nm [25]), *i.e.*, $\delta n_s = 0.0010$. From the simulation, it is observed that $\delta\theta_{SPR}$ marginally increases with an increase in MgF₂ thickness. More specifically, $\delta\theta_{SPR}$ varies from 0.0224° (for 50 nm thick MgF₂ layer) to 0.0229° (for 650 nm thick MgF₂ layer) leading to an almost constant sensitivity for any MgF₂ thickness considering, in particular, the fact that the available position detectors have resolution of the order of 0.001° only [39].

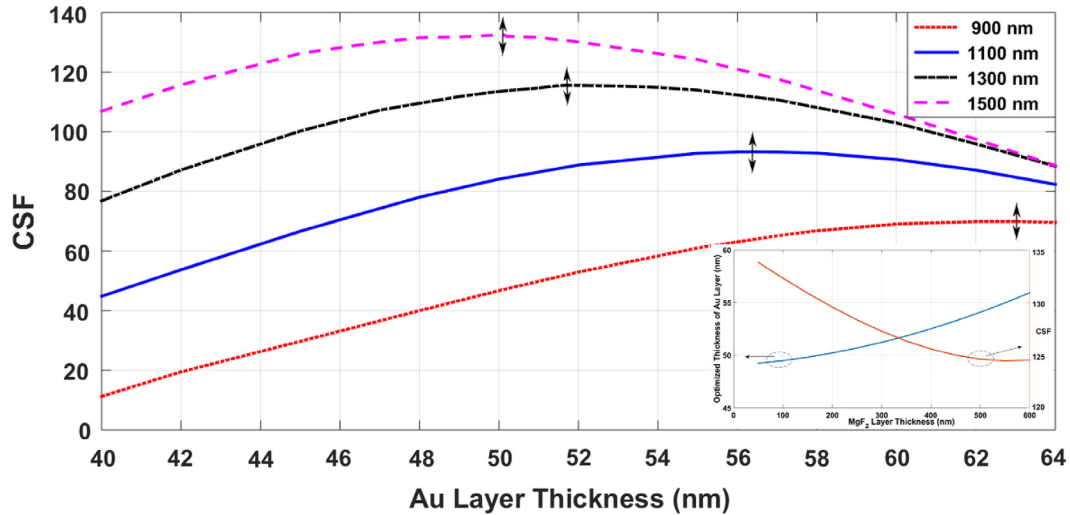


Fig. 3. Simulated variation of combined sensitivity factor (CSF) with Au layer thickness at four different NIR wavelengths (900 nm, 1100 nm, 1300 nm, and 1500 nm). The plots correspond to MgF_2 layer thickness of 200 nm and $\text{As}_{40}\text{Se}_{60}$ glass substrate. The analytes are considered to be H_2O and D_2O samples. The peak values marked (with double arrow) at each curve correspond to the Au thickness where maximum CSF is achieved for the concerned wavelength. The inset shows the simulated variations of (i) optimized Au thickness (on left hand vertical axis), and (ii) corresponding peak CSF (on right hand vertical axis) with MgF_2 layer thickness (varied between 50 nm and 600 nm) at $\lambda = 1500$ nm.

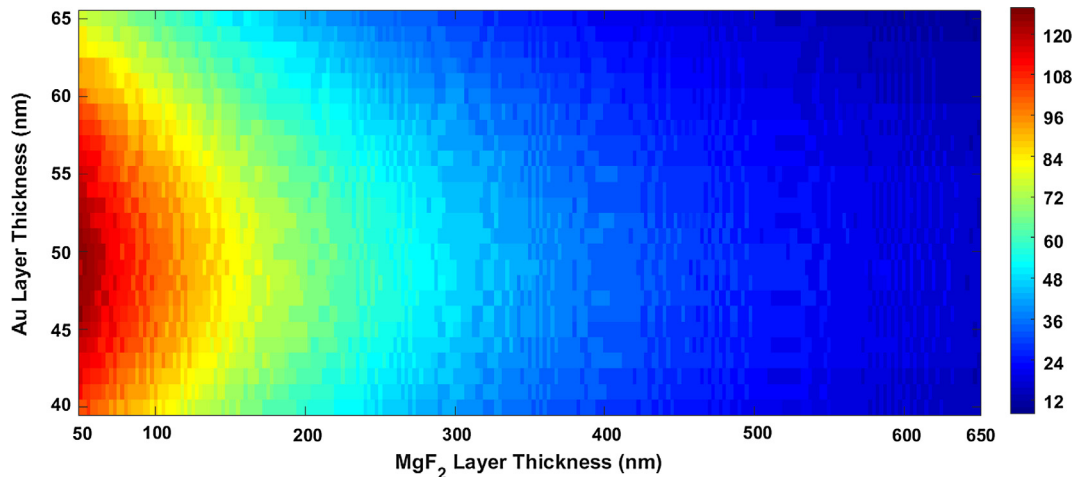


Fig. 4. Simulated variation of peak CSF as a two-dimensional function of Au and MgF_2 layers' thicknesses at $\lambda = 1500$ nm. The thickness of Au and MgF_2 layers are varied in the wide ranges of 40–65 nm and 50–650 nm, respectively.

The simulation results suggest that a detection limit of the order of nearly 10^{-6} RIU is achievable (considering an angular resolution $\sim 0.001^\circ$) with the proposed plasmonic sensor design at $\lambda = 1500$ nm. The previous studies show that operating in visible wavelength region leads to reasonably larger shift in plasmon resonance curve causing better detection limit [17]. However, it should also be kept in mind that in visible region, the resonance curve gets significantly broadened [20] leading to greater measurement error in addition to poorer suitability for biosample detection (due to photodamage [19]) compared with NIR wavelength.

3.2.2. R_{max} , R_{min} , and FWHM of resonance curve

It can be noted from Fig. 5 that as MgF_2 thickness is increased, corresponding resonance curve's dip (i.e., R_{min}) approaches zero, which indicates that the FWHM of resonance curve should increase with MgF_2 thickness due to lowering effect. The values of the corresponding FWHM mentioned in the bracket next to MgF_2 thickness vindicate the above observation. More precisely, the FWHM

of resonance curve varies from 0.134° (for 50 nm thick MgF_2 layer) to 0.214° (for 650 nm thick MgF_2 layer) indicating nearly 60% increase.

The resonance curve's uppermost (R_{max}) and bottom (R_{min}) points are also affected due to above lowering effect resulting from the variation in MgF_2 thickness. The inset of Fig. 4 presents the variations of R_{max} and R_{min} along with ' $R_{max} - R_{min}$ ' with MgF_2 thickness. As is visible, ' $R_{max} - R_{min}$ ' increases with MgF_2 thickness, however, it is important to gauge the extent of above increase because CSF is directly proportional to ' $R_{max} - R_{min}$ ' as per Eq. (9). Numerically, ' $R_{max} - R_{min}$ ' increases from 0.7291 (for 50 nm thick MgF_2 layer) to 0.9806 (for 650 nm thick MgF_2 layer) indicating nearly 34% increase. In this context, it is better to analyze the combined effect of ratio $(R_{max} - R_{min})/FWHM$ on CSF and it is found that the above ratio decays from nearly 5.5 (for 50 nm thick MgF_2 layer) to 4.5 (for 650 nm thick MgF_2 layer). Thus, in terms of the ratio $(R_{max} - R_{min})/FWHM$, the value of CSF should increase if thinner MgF_2 layer is employed.

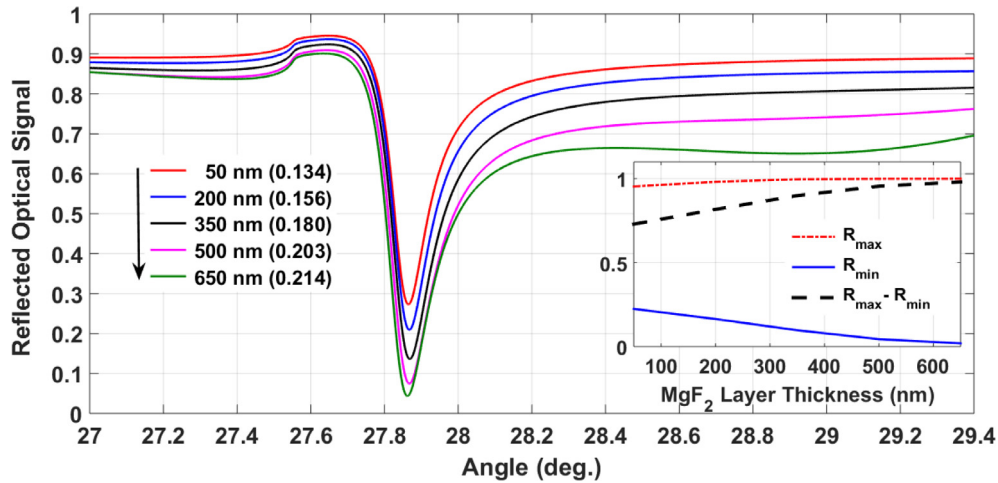


Fig. 5. Simulated resonance curves at $\lambda = 1500$ nm for five values (50 nm, 200 nm, 350 nm, 500 nm, and 650 nm) of MgF₂ layer thickness. The curves are plotted for Au layer of 50 nm thickness and As₄₀Se₆₀ glass substrate. For all five plots, D₂O sample is considered as analyte. The inset shows the corresponding variation of R_{\max} , R_{\min} , and ' $R_{\max} - R_{\min}$ ' with MgF₂ layer thickness. Also, the term mentioned in the bracket next to MgF₂ thickness represents the corresponding angular FWHM (in deg.) of resonance curve.

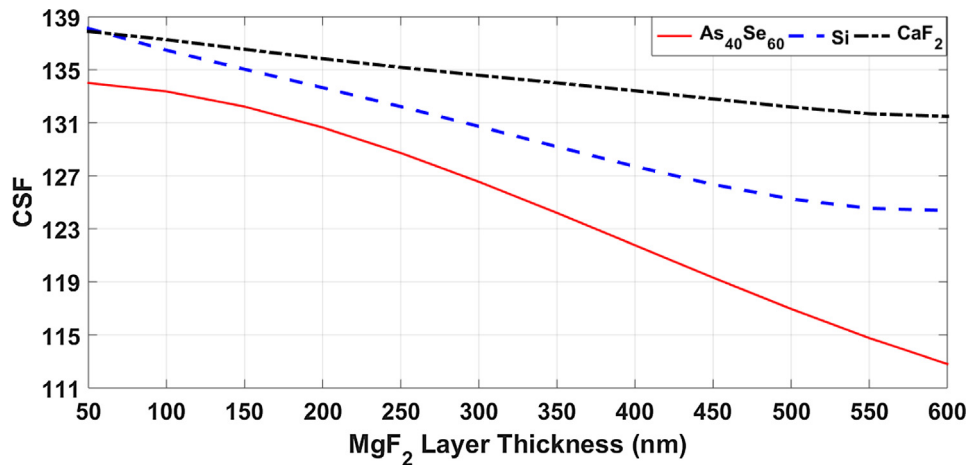


Fig. 6. Simulated variation of CSF with MgF₂ thickness for three different substrate materials (As₄₀Se₆₀, silicon, and CaF₂) at 1500 nm wavelength. The curves are plotted for Au layer of 50 nm thickness. D₂O sample is considered as analyte measured with reference to H₂O sample at room temperature.

3.2.3. Measurability of resonance curve

In addition to the effect of MgF₂ thickness on above-mentioned parameters, it is also important to comment on its effect on the measurability of resonance curve. Here, a perfectly measurable resonance curve is defined as the one which is as symmetric around the resonance dip (i.e., θ_{SPR}) as possible so that FWHM, R_{\max} , and R_{\min} can be measured accurately leading to correct estimation of sensor's CSF. It is also worthwhile to mention that the PWR effect becomes increasingly prominent with an increase in MgF₂ layer, which may lead to appearance of second resonance dip corresponding to plasmon waveguide mode. On the similar lines, it can be observed that the resonance curves depicted in Fig. 5 have variable symmetries depending on MgF₂ thickness. Clearly, the resonance curve's symmetry worsens with an increase in MgF₂ thickness, which can be described in terms of the plasmon penetration depth. At $\lambda = 1500$ nm, plasmon penetration depth in MgF₂ is nearly 1200 nm. Therefore, in a sensor design emphasizing on applying the SP mode only, a fine balance has to be struck and the MgF₂ thickness should be taken in such a way that the sufficiently strong interaction of SP mode with the analyte medium, which is attached adjacent to MgF₂ layer, may take place. If the

above interaction weakens, the coupling of SP mode with incident light will be weaker, which will have a direct effect on the shape of resonance curve leading to its deformation (or loss of symmetry) owing to appearance of PWR modes. Fig. 4 represents the same effect that as MgF₂ thickness approaches closer to the penetration depth, there is a loss of symmetry of resonance curve, which affects the measurability of resonance curve as discussed above. Thus, it poses another important constraint on the thickness of MgF₂ layer and the above discussion suggests that smaller MgF₂ thickness should be preferred, which is in concurrence with the result discussed in Section 3.2.2.

3.3. Performance variation among glass materials

Performance of a plasmonic sensor can be greatly affected by the glass material employed as light coupling substrate. In the introductory sections, As₄₀Se₆₀ chalcogenide glass was designated the role of light coupling substrate. However, better sensing performance at longer NIR wavelength (as discussed in Sections 3.1–3.2) prompts to consider other material substrates having suitable optical properties in NIR spectral region. The possible choices may be

fluoride glass and silicon. Among the fluoride glasses, CaF₂ (calcium fluoride) can be preferred due to high transparency, low RI, and large transmission window in NIR [40]. Similar favorable optical properties are shown by silicon in NIR and mid IR spectral regions [41]. In this context, Fig. 6 depicts the variation of CSF with MgF₂ thickness for three substrate materials (As₄₀Se₆₀, silicon, and CaF₂) at $\lambda = 1500$ nm in order to clearly observe the difference of their corresponding sensing performances.

It can be observed from the above figure that CaF₂ glass substrate is able to provide better sensing performance compared with other two substrates for most of the MgF₂ thickness values. At small MgF₂ thickness (in the vicinity of 50 nm), CSF for CaF₂ and silicon are almost identical but as the MgF₂ thickness is increased, the difference between their corresponding CSF values widens up. It is also important to note that CaF₂ substrate enables the significantly smaller variation in CSF for the whole range of MgF₂ thickness, which further consolidates that CaF₂ may be a better choice at longer NIR wavelength in order to achieve higher CSF values as well as to enable greater flexibility in choosing the suitable thickness of MgF₂ layer.

4. Conclusion

A detailed analysis of Au-MgF₂ based plasmonic sensor is carried out. After discussing the optimization of Au layer thickness vis-à-vis incident light wavelength and MgF₂ thickness, a detailed analysis of the effect of MgF₂ thickness on resonance curves simulated for concerned analyte samples (normal and heavy water) is carried out. It effectively exposes the reasons behind significant variation in sensor's overall performance that is analyzed in terms of CSF (in RIU⁻¹) for a range of MgF₂ thickness values. Further, it is found that taking large values of MgF₂ layer thickness may be avoided. Also, operating the sensor at longer NIR wavelength ensures more improved performance. Moreover, as another important result, it is found that fluoride glass substrates can provide better sensing performance compared with other infrared-active substrates such as chalcogenide glass and silicon substrate. It is worth-mentioning that the experimental values of refractive indices of different layers obtained by diverse groups under different preparation conditions have been used for simulation, therefore, under real experimental conditions, these values may vary and, hence, the practical performance of the proposed sensor may also be different from the simulation results reported in this study. The above differences may possibly be due to parameters such as temperature variation (leading to thermo-optic effect), the variation of wavelength measurement (leading to some dispersion effects), or errors in angle measurements. However, these effects are not expected to cause significant variation in the predicted (i.e., simulated) and actual performance of the proposed sensor.

Acknowledgment

The author gratefully acknowledges the Seed Research Grant (NITD/Dean(R&C)/16/35) funded by the National Institute of Technology Delhi.

Appendix A. Supplementary data

Supplementary data associated with this article can be found, in the online version, at <https://doi.org/10.1016/j.optlastec.2017.12.010>.

References

- [1] S. Enoch, N. Bonod, *Plasmonics: From Basic to Advanced Topics*, vol. 167, 2012.
- [2] R.C. Jorgenson, S.S. Yee, A fiber-optic chemical sensor based on surface plasmon resonance, *Sens. Actuat. B Chem.* 12 (1993) 213–220.
- [3] Y. Sun, Y. Xia, Increased sensitivity of surface plasmon resonance of gold nanoshells compared to that of gold solid colloids in response to environmental changes, *Anal. Chem.* 74 (2002) 5297–5305.
- [4] S.K. Ozdemir, G.T. Sayan, Temperature effects on surface plasmon resonance: design considerations for an optical temperature sensor, *J. Light. Technol.* 21 (3) (2003) 805–814.
- [5] H.A. Atwater, The promise of plasmonics, *Sci. Am.* 296 (4) (2007) 56–63.
- [6] Y. Yanase, T. Hiragun, T. Yanase, T. Kawaguchi, K. Ishii, M. Hide, Application of SPR imaging sensor for detection of individual living cell reactions and clinical diagnosis of type I allergy, *Allergol. Int.* 62 (2013) 163–169.
- [7] A.K. Sharma, G.J. Mohr, Plasmonic optical sensor for determination of refractive index of human skin tissues, *Sens. Actuat. B Chem.* 226 (2016) 312–317.
- [8] P.K. Maharana, T. Srivastava, R. Jha, Low index dielectric mediated surface plasmon resonance sensor based on graphene for near infrared measurements, *J. Phys. D: App. Phys.* 47 (38) (2014) 385102.
- [9] E. Kazuma, T. Tatsuma, Localized surface plasmon resonance sensors based on wavelength-tunable spectral dips, *Nanoscale* 6 (2014) 2397–2405.
- [10] S.A. Jung, T.S. Lee, W.M. Kim, K.S. Lee, D.S. Jeong, W.S. Lee, I. Kim, Thickness dependence of surface plasmon resonance sensor response for metal ion detection, *J. Phys. D: App. Phys.* 47 (38) (2013) 315104.
- [11] T. Wang, Y.Q. Xu, Photonic structure-integrated two-dimensional material optoelectronics, *Electronics* 93 (5) (2016) 2–18.
- [12] A. Bablich, S. Kataria, M. Lemme, Graphene and two-dimensional materials for optoelectronic, *Appl. Electron.* 5 (13) (2016) 1–16.
- [13] Y. Li, Z. Li, C. Chi, H. Shan, L. Zheng, Z. Fang, Plasmonics of 2D nanomaterials: properties and applications, *Adv. Sci.*, 1600430, 2017.
- [14] J.W. Weber, V.E. Calado, M.C.M.V.D. Sanden, Optical constants of graphene measured by spectroscopic ellipsometry, *Appl. Phys. Lett.* 97 (9) (2010) 091904.
- [15] A.R. Beal, H.P. Hughes, Kramers-Kronig analysis of the reflectivity spectra of 2H-MoSe₂, 2H-MoSe₂ and 2H-MoTe₂, *Solid State Phys.* 12 (1979) 881–890.
- [16] F. Bahrami, M. Maisonneuve, M. Meunier, An improved refractive index sensor based on genetic optimization of plasmon waveguide resonance, *Opt. Express* 21 (2013) 20863–20872.
- [17] Y. Zhou, P. Zhang, Y. He, Z. Xu, L. Liu, Y. Ji, H. Ma, Plasmon waveguide resonance sensor using an Au-MgF₂ structure, *Appl. Opt.* 53 (28) (2014) 6344–6350.
- [18] M.J. Dodge, Refractive properties of magnesium fluoride, *Appl. Opt.* 23 (1984) 1980–1985.
- [19] D. Kobat et al., Deep tissue multiphoton microscopy using longer wavelength excitation, *Opt. Express* 17 (16) (2009) 13354–13364.
- [20] B.P. Nelson et al., Near-infrared surface plasmon resonance measurements of ultrathin films. 1. Angle shift and SPR imaging experiments, *Anal. Chem.* 71 (1999) 3928–3934.
- [21] R. Ziblat et al., Infrared surface plasmon resonance: a novel tool for real time sensing of variations in living cells, *Biophys. J.* 90 (2006) 2592–2599.
- [22] V. Lirtsman et al., Infrared surface plasmon resonance technique for biological studies, *J. App. Phys.* 103 (2008) 014702.
- [23] B.H. Nguyen, V.H. Nguyen, Dispersion and attenuation of surface plasmon polariton at metal-dielectric interface, *Adv. Nat. Sci.: Nanosci. Nanotechnol.* 5 (2014) 035002.
- [24] E. Kretschmann, H. Raether, Radiative decay of non radiative surface plasmons excited by light, *Zeitschrift fur Naturforsch* 23 (1968) 2135–2136.
- [25] K. Johansen, H. Arwin, I. Lundstrom, B. Liedberg, Imaging surface plasmon resonance sensor based on multiple wavelengths: sensitivity considerations, *Rev. Scientific Instrumen.* 71 (9) (2000) 3530–3538.
- [26] B. Bureau, X.H. Zhang, F. Smeckala, J.L. Adam, J. Troles, H.L. Ma, C.B. Pledel, J. Lucas, P. Lucas, D.L. Coq, M.R. Riley, J.H. Simmons, Recent advances in chalcogenide glasses, *J. Non-Cryst. Solids* 345 (2004) 276–283.
- [27] SCHOTT Infrared Chalcogenide Glasses - IRG 26 Product flyer (Version May 2013).
- [28] A. Sarychev, D. Bergman, Y. Yagil, Theory of the optical and microwave properties of metal-dielectric films, *Phys. Rev. B* 51 (1995) 5366–5385.
- [29] P. Lecaruyer, M. Canva, J. Rolland, Metallic film optimization in a surface plasmon resonance biosensor by the extended Rouard method, *App. Opt.* 46 (12) (2007) 2361–2369.
- [30] S.A. Zynio, A. Samoylov, E. Surovtseva, V. Mirsky, Y. Shirshov, Bimetallic layers increase sensitivity of affinity sensors based on surface plasmon resonance, *Sensors* 2 (2) (2002) 62–70.
- [31] A.K. Sharma, B.D. Gupta, On the performance of different bimetallic combinations in surface plasmon resonance based fiber optic sensors, *J. App. Phys.* 101 (2007) 093111.
- [32] P. Jain, D. Arora, S.C. Bhatia, Surface plasmon resonance based recent advances in understanding plant development and related processes, *Biochem. Anal. Biochem.* 5 (2016) 300.
- [33] A.D. Rakić, A.B. Djurišić, J.M. Elazar, M.L. Majewski, Optical properties of metallic films for vertical-cavity optoelectronic devices, *Appl. Opt.* 37 (1998) 5271–5283.
- [34] E.D. Palik, *Handbook of Optical Constants of Solids*, Academic Press, 2012.

- [35] A. Feldman, D. Horowitz, R.M. Waxler, M.J. Dodge, Optical Materials Characterization Final Technical Report, 1979.
- [36] S. Kedenburg, M. Vieweg, T. Gissibl, H. Giessen, Linear refractive index and absorption measurements of nonlinear optical liquids in the visible and near-infrared spectral region, *Opt. Mater. Express* 2 (2012) 1588.
- [37] C.C. Katsidis, D.I. Siapkas, Systems with coherent, partially coherent, and incoherent interference, *Appl. Opt.* 41 (2002) 3978–3987.
- [38] A. Abbas, M.J. Linman, Q. Cheng, Sensitivity comparison of surface plasmon resonance and plasmon wave guide resonance biosensors, *Sens. Actuat. B: Chem.* 156 (2011) 169–175.
- [39] S. Cui, Y.C. Soh, Linearity indices and linearity improvement of 2-D tetralateral position-sensitive detector, *IEEE Trans. Electron. Devices* 57 (9) (2010) 2310–2316.
- [40] I.H. Malitson, A redetermination of some optical properties of calcium fluoride, *Appl. Opt.* 2 (11) (1963) 1103–1107.
- [41] M.A. Green, Self-consistent optical parameters of intrinsic silicon at 300 K including temperature coefficients, *Sol. Energ. Mat. Sol. Cells* 92 (2008) 1305–1310.